BRIEF COMMUNICATION OPEN

Check for updates

How much hydrogen is in green steel?

Özge Özgün[1], Xu Lu[2], Yan Ma[1]✉ and Dierk Raabe[1]✉

Hydrogen-based reduction of iron ores is the key technology for future sustainable ironmaking, to mitigate the CO_2 burden from the steel industry, accounting for ~7–8% of all global emissions. However, using hydrogen as a reductant prompts concerns about hydrogen embrittlement in steel products. This raises the question of how much hydrogen remains from green ironmaking in the metal produced. We answer this question here by quantifying the amount of hydrogen in iron produced via two hydrogen-based ironmaking processes, namely, direct reduction and plasma smelting reduction. Results suggest no threat of hydrogen embrittlement resulting from using hydrogen in green steel production.

npj Materials Degradation (2023)7:78 ; https://doi.org/10.1038/s41529-023-00397-8

Steel is the most important metallic material in terms of versatility (>3500 grades) and production quantity (1.95 billion tons in 2021[1]), serving in construction, energy conversion, infrastructure, transport, safety, and appliances, *etc*. However, the steel industry stands for about 7–8% of the global CO_2 emissions, making it the largest cause of global warming[2]. Particularly, the primary steel synthesis, responsible for about two thirds of today's global steel market, is highly CO_2-intensive owing to the use of fossil reductants (such as coal, coke, or natural gas) to reduce iron oxides[3]. It emits on average ~1.9 tons of CO_2 per ton of crude steel[4]. Because of the growing global steel demand and its longevity (often >50 years in construction and >25 years in machines[5]), the volume made via primary synthesis will remain on a similar level as today during the next decades. Thus, alternative synthesis methods with drastically reduced CO_2 emissions must be urgently developed to overcome the decarbonization challenge for steel[6].

Hydrogen-based reduction processes have qualified in recent years as possible alternatives, provided that a sufficient amount of green hydrogen is available and economically viable[7–9]. In this case, the by-product of the redox reaction is water. Hydrogen-based reduction works with solid and liquid oxides, where the former is referred to as hydrogen-based direct reduction (HyDR)[10] and the latter as hydrogen plasma smelting reduction (HPSR)[11]. In both processes, hydrogen not only reduces iron oxides but can also get trapped inside the produced metal. The latter effect has fueled concerns about the amount of hydrogen remaining in green steel, as even a few ppm of diffusible and weakly trapped hydrogen can have an enormously embrittling effect, particularly on advanced high-strength steels, leading to catastrophic failure[12,13]. This detrimental phenomenon, known as hydrogen embrittlement, has been studied for nearly 150 years[14]. Different mechanisms have been explored as possible causes for this effect[15], including hydrogen-enhanced localized plasticity[16,17], hydrogen-enhanced decohesion[18], hydrogen adsorption-induced dislocation emission[19], hydrogen-enhanced strain-induced vacancy formation[20]. For all these potential internal damaging mechanisms, the types of hydrogen traps inside the material are of high relevance[21]. Here, hydrogen traps refer to microstructural features, which absorb and capture hydrogen atoms[22].

Thus, the use of hydrogen creates a nexus between sustainable steel production and hydrogen embrittlement. This concern must be taken seriously because steel serves as the backbone material in safety-critical components and green steel that is not safe would be useless. Motivated by this conflict, we study here two key questions that need to be answered before implementing hydrogen as a reductant at the industrial scale for green steel production: (1) How much hydrogen is in green steel? (2) Will green steel suffer from severe hydrogen embrittlement? To answer these questions, we investigate the concentration of residual hydrogen in iron produced by hydrogen-based ironmaking processes using thermal desorption spectroscopy.

The HyDR on commercial direct-reduction hematite pellets was conducted at 900 °C under a pure hydrogen atmosphere using a thermogravimetry setup. After isothermal holding at this temperature for approximately 690 s, the reduction degree reached ~99%, suggesting completion of reduction, Fig. 1a. The XRD result confirmed that the HyDR product consisted of mainly α-Fe and a minor trace of magnetite (~1.5 wt.%), Fig. 1b. The typical microstructure of the HyDR product is shown in Fig. 1c. It revealed a porous structure, with a porosity of 45.0 ± 4.0%. The average size of the micro-pores was 2.97 ± 1.94 µm, and some nano-pores were also observed with an average size of 269 ± 167 nm (Fig. 1h). These acquired pores evolved during reduction due to the net volume loss caused by the removal of oxygen. Thus, the HyDR product is also called sponge iron. The elemental maps probed by energy-dispersive X-ray spectroscopy (e.g., Si, Al, Ca, and Mg in Fig. 1d–g, respectively) revealed the inherited gangue inclusions and their heterogeneous distribution in the HyDR product. Due to the thermodynamic constraints, i.e., their higher affinity to oxygen (compared with hydrogen and iron)[23], these elements were hardly reduced and remained as complex oxide compounds[24]. The grain size of the reduced sponge iron was in a wide range of 0.02–30.50 µm^2, as quantified using electron backscatter diffraction (see Supplementary Fig. 1). Low-angle grain boundaries (rotation angle <15°, composed of dislocation arrays) constituted the major type of planar defects with an area density of 0.61 µm/µm^2, while the density of high-angle grain boundaries (rotation angle >15°) was 0.19 µm/µm^2 (see Supplementary Fig. 1). Several high-angle grain boundaries are exemplarily shown in Fig. 1i. No dislocations were observed within the grain interior (Fig. 1i). All these observed microstructure defects, e.g., pores[25], residual magnetite[26], gangue oxides[27,28], high-angle grain boundaries[29–31], dislocations in low-angle grain boundaries[31], *etc*., could potentially

[1]Max-Plank-Institut für Eisenforschung, Max-Planck-Straße 1, 40237 Düsseldorf, Germany. [2]Department of Mechanical and Industrial Engineering, Norwegian University of Science and Technology, Richard Birkelands vei 2B, No-7491 Trondheim, Norway. ✉email: y.ma@mpie.de; d.raabe@mpie.de

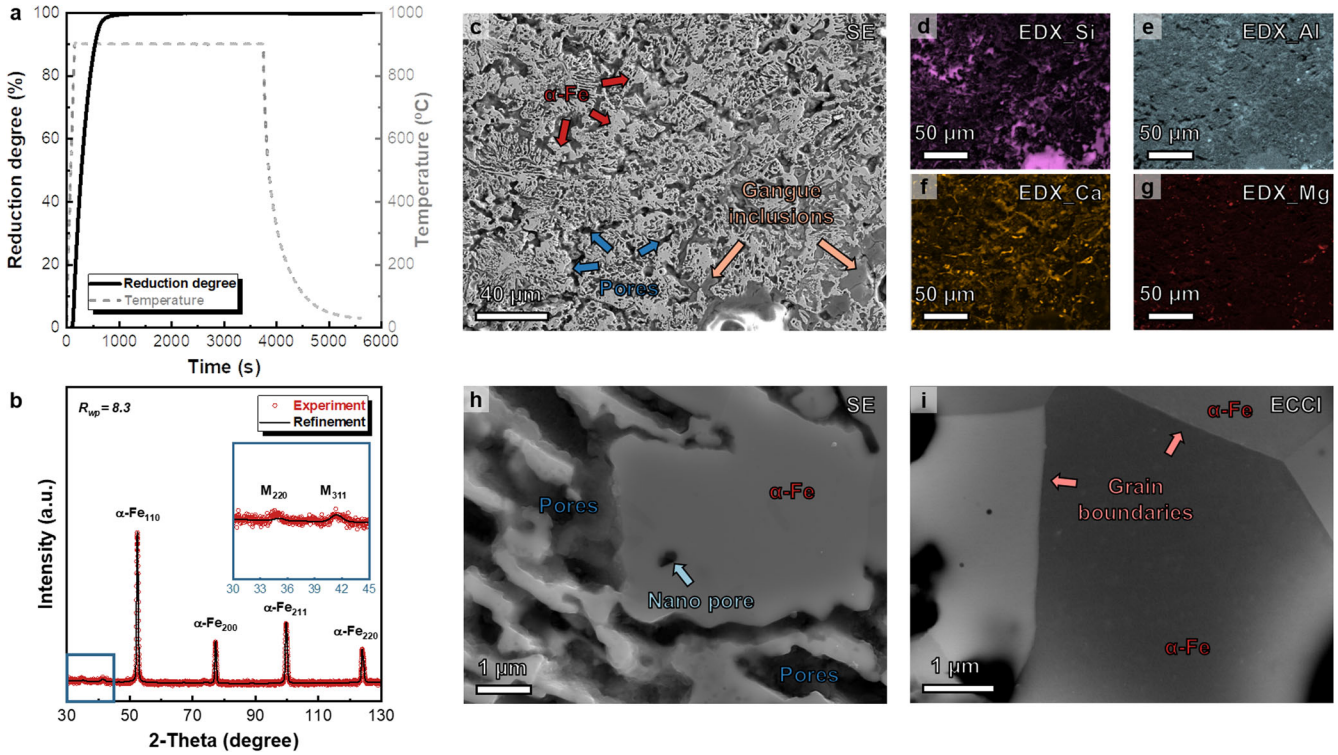

Fig. 1 Hydrogen-based direct reduction kinetics and microstructure of reduced iron. a Reduction degree of hydrogen-based direct reduction (HyDR) of a hematite pellet at 900 °C. **b** Phase identification from X-ray diffraction of the HyDR product (M stands for magnetite). **c** Secondary electron (SE) image of characteristic microstructure of reduced sponge iron. **d**–**g** Corresponding elemental maps of Si, Al, Ca, and Mg of (**c**) probed by energy-dispersive X-ray spectroscopy (EDX). **h** SE image highlighting a nano-pore. **i** Electron channeling contrast imaging (ECCI) showing high-angle grain boundaries.

trap hydrogen in the HyDR iron. After melting the sponge iron in an arc furnace, the solidified iron became compact (Supplementary Fig. 2). Some gangue inclusions (mainly SiO_2) with spherical morphology remained after melting, homogeneously distributed in the solidified iron. The HPSR product revealed a similar microstructure to the melted sponge iron (Supplementary Fig. 2).

Figure 2a shows the hydrogen desorption spectra of the samples during continuous heating at a ramping rate of 1000 °C/h. The HyDR product in its as-reduced solid state possessed the highest amount of hydrogen compared with the same sample after melting (HyDR+melt) and the HPSR product, as shown by the largest area below its desorption spectrum. By integrating the spectrum, the average hydrogen content in the HyDR product was evaluated to be 39.90 ± 9.00 wppm (Fig. 2b). The measurement results from both ramping (solid square) and rapid heating (open circle) tests were in good agreement. To identify the hydrogen trapping sites, the hydrogen desorption spectra were deconvoluted into four peaks, as shown in Fig. 2d for the ramping rate of 1000 °C/h. The activation energies of the individual peaks were determined to be 4.32 ± 0.31, 15.15 ± 4.10, 59.14 ± 20.13, and 126.07 ± 7.04 kJ/mol using the Kissinger method[32] (Fig. 2e, details in Supplementary Method section). These values correspond to the theoretically determined activation energies for (1) hydrogen desorbed from the body-centered cubic iron lattice[33,34] and hydrogen release from surface iron hydroxides; (2) high-angle grain boundaries and dislocations (constituting the low-angle grain boundaries)[35,36]; (3) nano-pore and iron oxide (Fe_3O_4)[28,37]; and (4) remaining gangue inclusions (e.g. SiO_2, Al_2O_3, etc.)[28], respectively (see Supplementary Table 1). Figure 2f shows the amount of hydrogen at these individual trapping sites. The results confirm that the complex defect substructures of the sponge iron offer multiple types of hydrogen trapping sites, capable of storing high amounts of hydrogen in the as-reduced HyDR solid-state material, namely, about 40 wppm.

When additionally melting the as-reduced HyDR product, its high hydrogen content drastically dropped to 1.46 ± 0.50 wppm (Fig. 2b), 96% below its value after the preceding solid-state reduction process. This additional melting step of the iron sponge is meant to mimic the subsequent steelmaking process where the sponge is transformed into a liquid, in an electric arc furnace or in a basic oxygen converter. Such a strong hydrogen removal effect can be attributed to: (1) outgassing of hydrogen from the liquid iron to the argon-filled furnace chamber, where the driving force comes from the difference in hydrogen concentration between liquid iron and the gas phase[38]; (2) removal of the relevant trapping sites of hydrogen during the melting process, such as pores (via liquefaction) and gangue oxides (via slag formation). The same principles also apply to the liquid-state HPSR process, explaining its very low hydrogen content of 0.98 ± 0.50 wppm.

During conventional metallurgical processes, hydrogen uptake from slag formers, air humidity, steel scrap, *etc*. can occur[38,39]. Its average content in hot metal ranges from 5–8 wppm processed through the blast furnace (BF), basic oxygen furnace (BOF), and electric arc furnace routes[40,41], which are the standard processes today. When deploying a subsequent vacuum degassing step, the hydrogen content can be reduced even further to 1–2 wppm[38]. As demonstrated in this study, green steel produced via hydrogen-based metallurgical reduction processes contains only 1–2 wppm hydrogen in its final liquid form, prior to its delivery to customers. This is a similar (low) level as steels processed via the currently most advanced (and expensive) vacuum degassing technology. Thus, the results suggest that using hydrogen in green steel production is not creating any threat of hydrogen embrittlement. However, hydrogen uptake in green steel can also occur in certain downstream processing and/or application environments, much

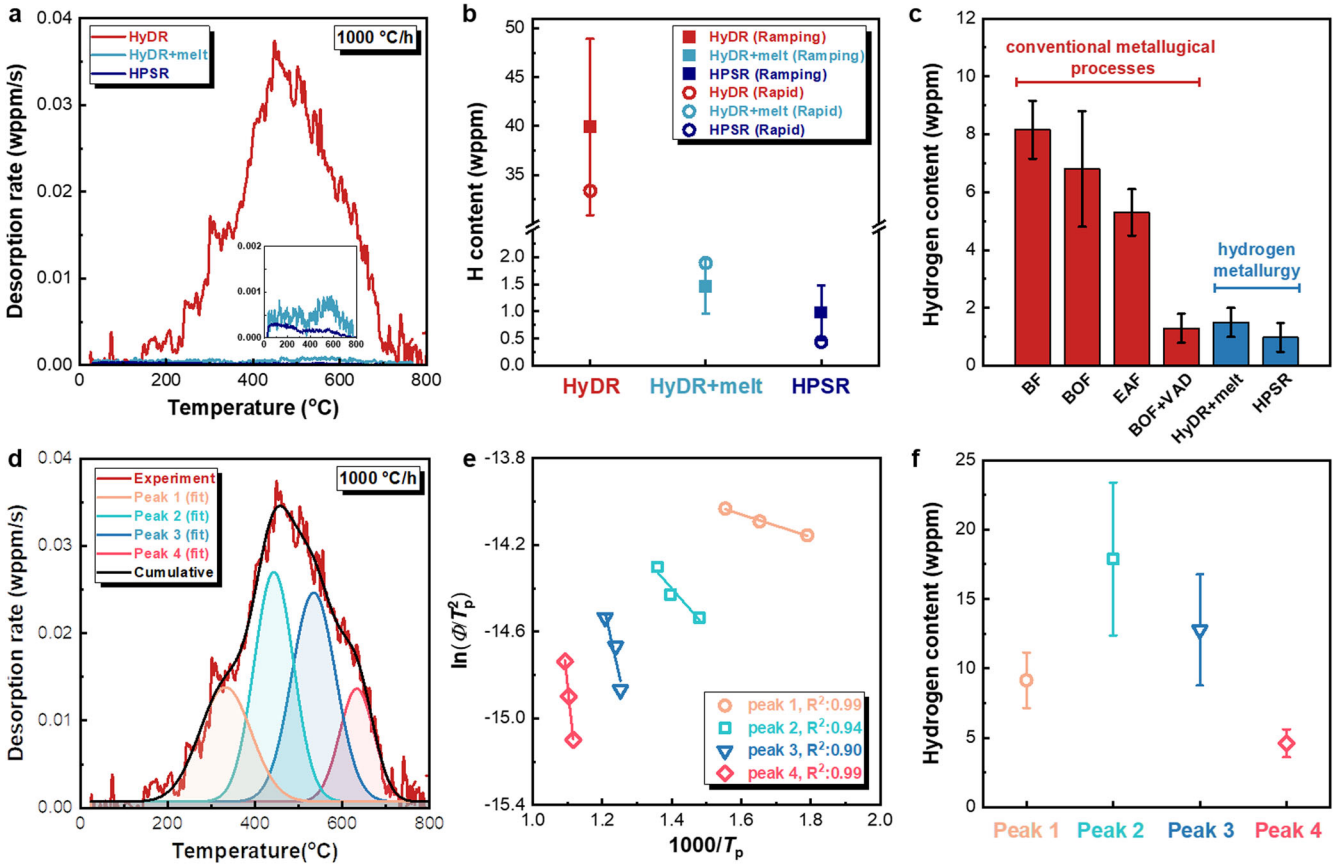

Fig. 2 Hydrogen uptake during hydrogen-based ironmaking processes. a Hydrogen desorption spectra of the HyDR, HyDR+melt, and HPSR samples measured by hot extraction tests with a constant ramping rate of 1000 °C/h. **b** Average hydrogen content (solid square) from measurements obtained for three constant ramping rates of 800, 1000, and 1200 °C/h. These values are denoted as 'Ramping'. The corresponding error bars represent the standard deviation from the three measurements. The figure shows for reference also the hydrogen content measured by rapid heating to 800 °C at a heating rate of ~800 °C/min (open circle), followed by isothermal holding for 15 min. This value is denoted as 'Rapid'. **c** Comparison of the hydrogen contents along the conventional metallurgical (BF stands for blast furnace, BOF for basic oxygen furnace, EAF for electric arc furnace, VAD for vacuum arc degassing) and hydrogen-based metallurgical processes. The corresponding error bars represent the standard deviation from data reported in the literature studies and measurements in the present study. **d** Deconvolution of hydrogen desorption spectrum of the HyDR product. **e**. Kissinger plots for the four deconvoluted peaks at ramping rates of 800, 1000, and 1200 °C/h, where T_p stands for the peak temperature of the deconvoluted peaks and Φ for the ramping rate. Details for the Kissinger method are in the Supplementary Method section. **f** Hydrogen contents corresponding to the four deconvoluted peaks.

like for any steel produced via the conventional BF-BOF route. This can happen for instance during pickling and galvanizing[42], storage and transport, when steel products are exposed to hydrogen-rich corrosive environments[42–45]. Yet, such downstream hydrogen uptake, which may in certain cases lead to hydrogen embrittlement in high-strength steels, is independent of the origin of the production of the raw material (conventional fossil fuel or green hydrogen as reductants). In either case, protective coatings and adequate microstructure design can be effective measures to improve the steels' resistance to hydrogen embrittlement[13,46].

In summary, we applied thermal desorption spectroscopy to evaluate the hydrogen content in virgin iron produced via two hydrogen-based ironmaking processes, namely, HyDR (solid-state reduction) and HPSR (liquid-state reduction). The complex defect structures in the HyDR sponge iron product trapped high amounts of hydrogen (~40 wppm). This high hydrogen content was drastically reduced by subsequent melting in an arc furnace, mainly through a degassing mechanism, to a level of 1–2 wppm. The HPSR product contained a very low hydrogen content of 0.98 ± 0.50 wppm immediately after the plasma smelting reduction. Compared with the steel produced via conventional processes followed by vacuum treatment (with a hydrogen content of 1–2 wppm), green steel produced via hydrogen-based ironmaking processes can reach a similar level of hydrogen. Thus, using hydrogen as a reductant for future sustainable steel production is not expected to be a cause of hydrogen embrittlement.

METHODS

Materials and process

Commercial hematite pellets were used in this study. HyDR was conducted in a laboratory thermogravimetry analysis set-up[47]. The pellets were exposed to pure hydrogen gas (purity of 99.999%) at 900 °C for 1 h. The heating rate was 5 °C/s. The flow rate of hydrogen gas was 30 L/h. The details of hematite pellets and the HyDR procedures were described elsewhere[48]. Subsequently, ~6 grams of HyDR product were melted in an arc furnace (inner volume of 18 L) with a tungsten electrode under the pure Ar atmosphere for three times. Each melting cycle lasted for 65 s. Moreover, hematite pellets (~12 g) were processed by HPSR in the same arc furnace with a gas mixture of Ar–10%H_2 at a total pressure of 900 mbar, which was operated in 15 cycles. In each cycle, the sample was exposed to an electric arc with hydrogen plasma for one minute. The pellets were simultaneously melted and reduced. After individual cycles, the furnace chamber was replenished with the fresh gas mixture[49].

Microstructural characterization

Disc-shaped specimens with a thickness of 1.0–1.5 mm were sliced from the middle of the produced iron using a diamond wire saw. The surfaces were ground with SiC papers down to 4000 grit. Subsequently, the surfaces were polished using diamond suspensions with a particle size of 3 µm and 1 µm, followed by final polishing using colloidal silica suspension (OPS). The microstructure of samples was characterized using a Zeiss Merlin scanning electron microscope (SEM). The 2D porosity analysis of the HyDR sample was performed on 15 SE images using ImageJ software for statistics. The elemental distribution was probed by energy-dispersive X-ray spectroscopy (EDX). In addition, electron backscatter diffraction (EBSD) was conducted to characterize the crystallographic information (e.g., grain size and types of grain boundaries). The step size of the EBSD measurement was 100 nm and the EBSD data were analyzed using the software OIM Analysis™ V8.6. Further, X-ray diffraction (XRD) analysis was employed to identify the phases using Seifert Theta/Theta diffractometer equipped with cobalt K_α radiation. The phase fractions were quantified by the Rietveld refinement method using the Material Analysis Using Diffraction (MAUD) software[50].

Thermal desorption spectroscopy (TDS)

To quantify hydrogen content and to investigate hydrogen trapping behavior in different samples, TDS measurements were conducted using G4 Pheonix DH equipment (Bruker Co.). The samples were heated up to 800 °C using an infrared furnace with either three constant heating rates (i.e., 800, 1000, and 1200 °C/h) or a rapid heating procedure (within 1 min). A mass spectrometer precisely recorded the current flow of desorbed hydrogen, and the integration of this current flow yielded the total hydrogen content. The gap between the sample preparation and the measurement of hydrogen content was about two to four weeks. This period concurs with the shipment or storage durations of the semi-products (here, sponge iron) usually for downstream processing.

DATA AVAILABILITY

The data presented in this article are available upon request to the authors.

Received: 19 May 2023; Accepted: 13 September 2023;
Published online: 02 October 2023

REFERENCES

1. https://worldsteel.org/wp-content/uploads/World-Steel-in-Figures-2022-1.pdf World Steel in Figures (2022) (accessed: 2023/04/11).
2. Raabe, D., Tasan, C. C. & Olivetti, E. A. Strategies for improving the sustainability of structural metals. *Nature* **575**, 64–74 (2019).
3. Ma, Y. et al. Reducing iron oxide with ammonia: a sustainable path to green steel. *Adv. Sci.* **10**, 2300111 (2023).
4. Flores-Granobles, M. & Saeys, M. Minimizing CO2 emissions with renewable energy: a comparative study of emerging technologies in the steel industry. *Energy Environ. Sci.* **13**, 1923–1932 (2020).
5. Cooper, D. R., Skelton, A. C. H., Moynihan, M. C. & Allwood, J. M. Component level strategies for exploiting the lifespan of steel in products. *Resour. Conserv. Recycl.* **84**, 24–34 (2014).
6. Raabe, D. The materials science behind sustainable metals and alloys. *Chem. Rev.* **123**, 2436–2608 (2023).
7. Wang, R. R., Zhao, Y. Q., Babich, A., Senk, D. & Fan, X. Y. Hydrogen direct reduction (H-DR) in steel industry—an overview of challenges and opportunities. *J. Clean. Prod.* **329**, 129797 (2021).
8. Tang, J. et al. Development and progress on hydrogen metallurgy. *Int. J. Miner. Metall. Mater.* **27**, 713–723 (2020).
9. Cavaliere, P., Perrone, A., Marsano, D. & Primavera, V. Hydrogen-based direct reduction of iron oxides pellets modeling. *Steel Res. Int.* **94**, 2200791 (2023).
10. Ma, Y. et al. D. Hierarchical nature of hydrogen-based direct reduction of iron oxides. *Scr. Mater.* **213**, 114571 (2022).
11. Naseri Seftejani, M., Schenk, J. & Zarl, M. A. Reduction of haematite using hydrogen thermal plasma. *Materials* **12**, 1608 (2019).
12. Bhadeshia, H. K. D. H. Prevention of hydrogen embrittlement in steels. *ISIJ Int* **56**, 24–36 (2016).
13. Sun, B. et al. Current challenges and opportunities toward understanding hydrogen embrittlement mechanisms in advanced high-strength steels: a review. *Acta Metall. Sin. (Engl. Lett.)* **34**, 741–754 (2021).
14. Johnson, W. H. On some remarkable changes produced in iron and steel by the action of hydrogen and acids. *Proc. R. Soc. Lond.* **23**, 168–179 (1875).
15. Robertson, I. M. et al. Hydrogen embrittlement understood. *Metall. Mater. Trans. B* **46**, 1085–1103 (2015).
16. Beachem, C. D. A new model for hydrogen-assisted cracking (hydrogen "embrittlement"). *Metall. Trans.* **3**, 441–455 (1972).
17. Huang, L. et al. Quantitative tests revealing hydrogen-enhanced dislocation motion in α-iron. *Nat. Mater.* **22**, 710–716 (2023).
18. Oriani, R. A. A mechanistic theory of hydrogen embrittlement of steels. *Ber. Bunsenges. Phys. Chem.* **76**, 848–857 (1972).
19. Lynch, S. Hydrogen embrittlement phenomena and mechanisms. *Corros. Rev.* **30**, 105–123 (2012).
20. Nagumo, M., Ohta, K. & Saitoh, H. Deformation induced defects in iron revealed by thermal desorption spectroscopy of tritium. *Scr. Mater.* **40**, 313–319 (1999).
21. Ma, M.-T. et al. Hydrogen embrittlement of advanced high-strength steel for automobile application: a review. *Acta Metall. Sin. (Engl. Lett.)* **36**, 1144–1158 (2023).
22. Koyama, M. et al. Recent progress in microstructural hydrogen mapping in steels: quantification, kinetic analysis, and multi-scale characterisation. *Mater. Sci. Technol.* **33**, 1481–1496 (2017).
23. Ellingham, H. J. T. Reducibility of oxides and sulphides in metallurgical processes. *J. Soc. Chem. Ind.* **63**, 125–160 (1944).
24. Spreitzer, D. & Schenk, J. Reduction of iron oxides with hydrogen—a review. *Steel Res. Int.* **90**, 1900108 (2019).
25. Choo, W. Y. & Lee, J. Y. Thermal-analysis of trapped hydrogen in pure iron. *Metall. Trans. A* **13**, 135–140 (1982).
26. Hong, G. W. & Lee, J. Y. The interaction of hydrogen with iron-oxide inclusions in iron. *Mater. Sci. Eng.* **61**, 219–225 (1983).
27. Lee, J. L. & Lee, J. Y. The interaction of hydrogen with the interface of Al_2O_3 particles in iron. *Metall. Trans. A* **17**, 2183–2186 (1986).
28. Lee, K. Y., Lee, J. Y. & Kim, D. R. A study of hydrogen-trapping phenomena in AISI 5160 spring steel. *Mater. Sci. Eng.* **67**, 213–220 (1984).
29. Oudriss, A. et al. Grain size and grain-boundary effects on diffusion and trapping of hydrogen in pure nickel. *Acta Mater.* **60**, 6814–6828 (2012).
30. Sato, R. & Takai, K. Quantitative hydrogen trap states on high-angle grain boundaries and at dislocations in iron. *Scr. Mater.* **228**, 115339 (2023).
31. Chen, Y.-S. et al. Observation of hydrogen trapping at dislocations, grain boundaries, and precipitates. *Science* **367**, 171–175 (2020).
32. Kissinger, H. E. Reaction kinetics in differential thermal analysis. *Anal. Chem.* **29**, 1702–1706 (1957).
33. Hayward, E. & Fu, C.-C. Interplay between hydrogen and vacancies inα-Fe. *Phys. Rev. B* **87**, 174103 (2013).
34. Jiang, D. E. & Carter, E. A. Diffusion of interstitial hydrogen into and through bcc Fe from first principles. *Phys. Rev. B* **70**, 064102 (2004).
35. Vandewalle, L., Konstantinović, M. J., Verbeken, K. & Depover, T. A combined thermal desorption spectroscopy and internal friction study on the interaction of hydrogen with microstructural defects and the influence of carbon distribution. *Acta Mater.* **241**, 118374 (2022).
36. Lee, J.-Y. & Lee, J.-L. A trapping theory of hydrogen in pure iron. *Philos. Mag. A* **56**, 293–309 (1987).
37. Lee, J. & Lee, J. Y. Hydrogen trapping in AISI 4340 steel. *Met. Sci.* **17**, 426–432 (1983).
38. Holappa, L. In *Treatise on Process Metallurgy* 3 (ed S. Seetharaman) (Elsevier, 2014).
39. Turkdogan, E. T. *Fundamentals of Steelmaking*. (Institute of Materials, 1996).
40. Starshinov, B. N. et al. Improving the properties of foundry-grade pig iron. *Metallurgist* **16**, 96–99 (1972).
41. Vrbek, K., Lamut, J., Marolt, M. & Knap, M. Changes in hydrogen content during steelmaking. *Arch. Metall. Mater.* **60**, 295–299 (2015).
42. Shirband, Z., Shishesaz, M. R. & Ashrafi, A. Hydrogen degradation of steels and its related parameters, a review. *Ph. Transit.* **84**, 924–943 (2011).
43. Yan, Y. et al. Hydrogen-induced cracking and service safety evaluation for precipitation strengthened austenitic stainless steel as hydrogen storage tank. *Int. J. Hydrog. Energy* **39**, 17921–17928 (2014).
44. Wan, D. et al. Evaluation of hydrogen effect on the fatigue crack growth behavior of medium-Mn steels via in-situ hydrogen plasma charging in an environmental scanning electron microscope. *J. Mater. Sci. Technol.* **85**, 30–43 (2021).
45. Lu, X. et al. Insight into hydrogen effect on a duplex medium-Mn steel revealed by in-situ nanoindentation test. *Int. J. Hydrog. Energy* **44**, 20545–20551 (2019).

46. Sun, B. et al. Chemical heterogeneity enhances hydrogen resistance in high-strength steels. *Nat. Mater.* **20**, 1629–1634 (2021).
47. Auinger, M., Vogel, D., Vogel, A., Spiegel, M. & Rohwerder, M. A novel laboratory set-up for investigating surface and interface reactions during short term annealing cycles at high temperatures. *Rev. Sci. Instrum.* **84**, 085108 (2013).
48. Kim, S.-H. et al. Influence of microstructure and atomic-scale chemistry on the direct reduction of iron ore with hydrogen at 700°C. *Acta Mater.* **212**, 116933 (2021).
49. Souza Filho, I. R. et al. Sustainable steel through hydrogen plasma reduction of iron ore: process, kinetics, microstructure. *Chem. Acta Mater.* **213**, 116971 (2021).
50. Lutterotti, L. Total pattern fitting for the combined size–strain–stress–texture determination in thin film diffraction. *Nucl. Instrum. Methods Phys. Res. B* **268**, 334–340 (2010).

ACKNOWLEDGEMENTS

This work has been performed in the framework of the International Max Planck Research School for Sustainable Metallurgy (IMPRS SusMet). Y.M. is grateful for the financial support through the Walter Benjamin Programme of the Deutsche Forschungsgemeinschaf (project No. 468209039). D.R. is grateful for the financial support through the ERC Advanced grant ROC (grant agreement No 101054368). Views and opinions expressed are however those of the author(s) only and do not necessarily reflect those of the European Union and the ERC. Neither the European Union nor the granting authority can be held responsible for them. X.L acknowledges the financial support from The Research Council of Norway through the research center HYGROGENi (333118). The authors thank Annika Laimmer, Benjamin Breitbach, and Michael Kulse for their support of TGA, XRD experiments and melting reduced samples, respectively. Christian Broß and Katja Angenendt are acknowledged for their support of the metallography lab and SEM facilities at MPIE. Prof. Abdelali Oudriss is gratefully acknowledged for the discussion on TDS results.

AUTHOR CONTRIBUTIONS

Y.M. and D.R. conceived the project. Ö.Ö. conducted the reduction experiments. X.L. performed the TDS measurements. Ö.Ö. conducted the microstructure characterization. All authors discussed the results and wrote the manuscript.

FUNDING

Open Access funding enabled and organized by Projekt DEAL.

COMPETING INTERESTS

The authors declare no competing interests.

ADDITIONAL INFORMATION

Supplementary information The online version contains supplementary material available at https://doi.org/10.1038/s41529-023-00397-8.

Correspondence and requests for materials should be addressed to Yan Ma or Dierk Raabe.

Reprints and permission information is available at http://www.nature.com/reprints

Publisher's note Springer Nature remains neutral with regard to jurisdictional claims in published maps and institutional affiliations.